Optics Letters

Efficient type II second harmonic generation in an indium gallium phosphide on insulator wire waveguide aligned with a crystallographic axis

NICOLAS POULVELLARIE,[1,2,3,*] CARLOS MAS ARABI,[1] CHARLES CIRET,[4] SYLVAIN COMBRIÉ,[5] ALFREDO DE ROSSI,[5] MARC HAELTERMAN,[1] FABRICE RAINERI,[6,7] BART KUYKEN,[2,3] SIMON-PIERRE GORZA,[1] AND FRANÇOIS LEO[1]

[1]OPERA-Photonique, Université libre de Bruxelles, Brussels, Belgium
[2]Photonics Research Group, Ghent University-IMEC, Ghent, Belgium
[3]Center for Nano and Biophotonics (NB-Photonics), Ghent University-IMEC, Ghent, Belgium
[4]Laboratoire de Photonique d'Angers EA 4464, Université d'Angers, Angers, France
[5]Thalès Research and Technology, Palaiseau, France
[6]Centre de Nanosciences et de Nanotechnologies (C2N), CNRS, Université Paris Sud, Université Paris Saclay, F-91120 Palaiseau, France
[7]Université de Paris, Centre de Nanosciences et de Nanotechnologies (C2N), F-91120 Palaiseau, France
*Corresponding author: Nicolas.Poulvellarie@ulb.be

Received 18 December 2020; revised 19 February 2021; accepted 23 February 2021; posted 23 February 2021 (Doc. ID 418064); published 17 March 2021

We theoretically and experimentally investigate type II second harmonic generation in III-V-on-insulator wire waveguides. We show that the propagation direction plays a crucial role and that longitudinal field components can be leveraged for robust and efficient conversion. We predict that the maximum theoretical conversion is larger than that of type I second harmonic generation for similar waveguide dimensions and reach an experimental conversion efficiency of 12%/W, limited by the propagation loss.

https://doi.org/10.1364/OL.418064

Second harmonic generation (SHG) was first demonstrated almost 60 years ago [1] and still attracts a lot of attention. In particular, many novel integrated platforms for integrated SHG have recently emerged [2–4]. Conversions as high as $47{,}000\%/(\mathrm{W}\cdot\mathrm{cm}^2)$ have been demonstrated in III-V semiconductors [5], and ultra-wide tuning was recently shown in silicon waveguides [6]. The large intrinsic nonlinearity in addition to the high-index contrast of sub-wavelength structures leads to very large effective nonlinearities. Different schemes for phase matching have been proposed and implemented [7–9]. Type I modal phase matching, consisting of engineering the waveguide cross section such that a pump mode and a SH higher-order mode propagate at the same phase velocity, is attractive because standard waveguiding structures can be used. It, however, leads to lower conversion efficiency as compared to other schemes because of the sub-optimal overlap between the pump and SH mode in the nonlinear core of the waveguide. Record conversions in gallium arsenide wire waveguides were recently reported by optimizing such overlap. But the efficiency is still limited because very thin layers are used to ensure phase matching between two fundamental modes [5]. Moreover, it makes the conversion very sensitive to fabrication variations.

Here we show that type II SHG can help alleviate these limitations. We theoretically analyze the nonlinear conversion with a full-vectorial model to identify the most efficient configurations and experimentally confirm our predictions in indium gallium phosphide (InGaP) nanowires.

To the best of our knowledge, type II SHG has never been demonstrated in the strong-guidance regime. It was previously studied in AlGaAs photonic wires with low vertical confinement [10], where the modes are well approximated by transverse waves. As we recently demonstrated for the case of type I SHG, more complex wave mixing involving the longitudinal components can be expected in III-V-on-insulator wire waveguides [11,12]. We hence apply the same vectorial analysis to the case of type II phase matching to identify efficient nonlinear couplings between a pump around 1550 nm and a higher-order mode around 775 nm.

We write the electric field as a superposition of three forward propagating bound modes, two oscillating at ω_0 and one at $2\omega_0$, in the waveguide frame (xyz), where x is the horizontal coordinate, y the vertical coordinate, and z the propagation direction (Fig. 2). The total electric field reads

$$\boldsymbol{E} = a_1(z)\boldsymbol{e}_{a_1}(\mathbf{r}_\perp, \omega_0)e^{i(\beta_{a_1}z-\omega_0 t)} + a_2(z)\boldsymbol{e}_{a_2}(\mathbf{r}_\perp, \omega_0)e^{i(\beta_{a_2}z-\omega_0 t)} + b(z)\boldsymbol{e}_b(\mathbf{r}_\perp, 2\omega_0)e^{i(\beta_b z-2\omega_0 t)} + \text{c.c.}, \tag{1}$$

where a_1 and a_2 represent the amplitudes of both pump modes and b the amplitude of the SH mode (expressed in $\sqrt{W}$). β_{a_1}, β_{a_2} are the propagation constants at carrier frequency ω_0, and β_b is the propagation constant at carrier frequency $2\omega_0$. $\boldsymbol{e}_{a1,a2}(x, y, \omega_0)$ and $\boldsymbol{e}_b(x, y, 2\omega_0)$ are the orthonormal vectorial electric profiles of the modes. They satisfy the usual orthonormality condition [13].

The propagation equations can be found through perturbation theory [14–16]. Here we retain only the nonlinear terms involving three different modes and include the propagation loss. We find

$$\frac{da_1}{dz} = -\frac{\alpha_{a_1}}{2} a_1 + i\kappa_{12}^* b a_2^* \exp(-i\Delta\beta z),$$
$$\frac{da_2}{dz} = -\frac{\alpha_{a_2}}{2} a_2 + i\kappa_{12}^* b a_1^* \exp(-i\Delta\beta z),$$
$$\frac{db}{dz} = -\frac{\alpha_b}{2} b + 2i\kappa_{12} a_1 a_2 \exp(i\Delta\beta z), \quad (2)$$

where α_{a_1}, α_{a_2}, and α_b are the linear loss coefficients of the respective modes, and $\Delta\beta = \beta_{a1} + \beta_{a2} - \beta_b$ is the wavenumber mismatch. The effective nonlinearity κ_{12}, expressed in $(\sqrt{\mathrm{W}} \cdot \mathrm{m})^{-1}$, reads

$$\kappa_{12} = \omega_0 \varepsilon_0 \iint_A \sum_{jkl=xyz} \chi_{jkl}^{(2)} e_b^{*j} e_{a_1}^k e_{a_2}^l \mathrm{d}x\mathrm{d}y, \quad (3)$$

with ε_0 the vacuum permittivity and A the nonlinear waveguide core. We recall that Eq. (2) is written in the waveguide frame such that the nonlinear tensor elements are dependent on the propagation direction. In the crystal frame of a III-V semiconductor, only the $j \neq k \neq l$ elements are nonzero. To account for other directions, the nonlinear tensor must be rotated (see, e.g., [10]). Most III-V wafers are grown along a crystallographic axis. Here we consider the case of a wafer grown along the [10] axis and use the [100] direction as the reference in the propagation plane.

In the undepleted regime, the SH output power can be found analytically. We neglect the parametric down conversion terms and integrate Eq. (2) along the propagation direction. We find

$$P_{\mathrm{sh}} = 16|\kappa_{12}|^2 \frac{P_1 P_2}{|\Phi|^2} \left|\sinh\left(\frac{\Phi}{2} z\right)\right|^2 \exp\left[-\left(\frac{\alpha_b}{2} + \alpha_a\right) z\right], \quad (4)$$

where $\alpha_{a_1} = \alpha_{a_2} = \alpha_a$, and $\Phi = \alpha_b/2 - \alpha_a + i\Delta\beta$. $P_{1,2} = |E_{1,2}|^2$ are the input powers at the pump wavelength. To maximize the conversion, we set $P_1 = P_2 = P_0/2$, with P_0 the total input power. The maximum output power, found by setting $\Delta\beta = 0$, can then be written as $P_{\mathrm{sh}}(L) = |\kappa P_0 L_{\mathrm{eff}}|^2$, where

$$L_{\mathrm{eff}} = 2\frac{\exp(-\alpha_a L) - \exp(-\alpha_b L/2)}{\alpha_b - 2\alpha_a}, \quad (5)$$

and L is the length of the waveguide. This is the same expression as that of type I SHG [11]. In what follows, we use the effective nonlinearity κ_{12} to compare different configurations as well as to confront our experimental results with theoretical predictions.

We now look for specific cases of phase matching to evaluate the theoretical conversion efficiency in standard waveguides. We consider fully etched InGaP-on-insulator wire waveguides with a 200 nm hydrogen silsesquioxane (HSQ) cladding layer. The refractive index of HSQ is similar to that of silicon dioxide. The layout corresponds to the waveguides used in the experiment discussed below. InGaP possesses a single nonzero second-order nonlinear coefficient that was measured to be as high as $\chi_{xyz}^{(2)} = 220$ pm/V [17]. In principle, any two pump modes can be used for type II SHG, but wave mixing processes involving the two fundamental modes (TE_{00} and TM_{00}) are expected to be the most efficient. Moreover, it is the easiest scheme to implement experimentally in sub-wavelength waveguides with free-space injection. We hence look for phase matching between the two fundamental modes around 1550 nm and a higher-order mode around 775 nm. We vary the width and height of the waveguide in steps of 5 nm in each direction. When a phase matching point is found in a 10 nm window around the 1550 nm wavelength, we compute the efficiency as a function of the propagation direction (either 0° or 45°) and place a marker in the efficiency map shown in Fig. 1.

The marker color codes the relative strength of the coupling, and its shape indicates the propagation direction for which it is maximized: squares correspond to 0° waveguides, while diamonds represent 45° waveguides. To limit the computational time, we restrict the simulations to widths between 600 and 1000 nm and heights between 100 and 400 nm. We connect the markers corresponding to the same SH higher-order mode with a line. Interestingly, and in contrast to type I SHG [12], the most efficient conversion occurs for relatively thick waveguides (605 nm wide, 295 nm high) aligned with a main crystallographic axis [$\kappa_{\max} = i3500\ (\mathrm{W}^{1/2} \cdot \mathrm{m})^{-1}$]. For comparison, the maximum found for type I SHG in the same range of waveguide dimensions is $\kappa_1 = 2816\ (\mathrm{W}^{1/2} \cdot \mathrm{m})^{-1}$ [12]. The higher efficiency for type II SHG can be understood by analyzing the expression of the effective nonlinearity for waves propagating along a crystallographic axis of a III-V material. It reads

$$\kappa_{12} = \omega_0 \varepsilon_0 \iint_A \chi_{xyz}^{(2)} [e_b^{*x}(e_{a_1}^y e_{a_2}^z + e_{a_1}^z e_{a_2}^y) + e_b^{*y}(e_{a_1}^z e_{a_2}^x + e_{a_1}^x e_{a_2}^z) + e_b^{*z}(e_{a_1}^x e_{a_2}^y + e_{a_1}^y e_{a_2}^x)]\mathrm{d}x\mathrm{d}y, \quad (6)$$

where $\chi_{xyz}^{(2)}$ is the single nonzero tensor element of InGaP. In the specific case of predominant TM_{00} and TE_{00} pump modes and a TM higher-order mode at the SH, Eq. (6) can be approximated by the simpler expression

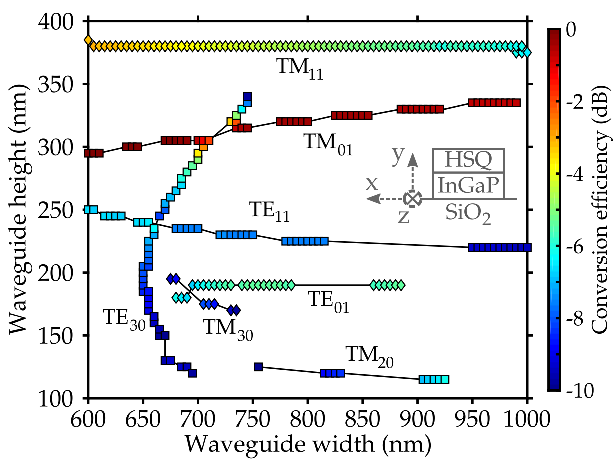

Fig. 1. Efficiency map of the nonlinear coupling between TE_{00} and TM_{00} pump modes and a higher order second harmonic mode of an InGaP-on-insulator wire waveguide. Only phase-matched interactions are shown. Squares (diamonds) correspond to a waveguide rotated at 0° (45°) from the [100] crystallographic axis. The conversion efficiency is normalized to the maximum value $[(|\kappa|/|\kappa_{\max}|)^2$ (dB), with $\kappa_{\max} = i3500\ (\mathrm{W}^{1/2} \cdot \mathrm{m})^{-1}]$.

$$\kappa_{12} \approx \omega_0 \varepsilon_0 \iint_A \chi^{(2)}_{xyz} e^x_{a_1} (e^{*y}_b e^z_{a_2} + e^{*z}_b e^y_{a_2}) \mathrm{d}x\mathrm{d}y. \quad (7)$$

The effective nonlinearity is dominated by two terms, both involving a longitudinal electric field component. A transverse mode approximation would yield no conversion in this case. The wave mixing process involving longitudinal components does not preclude efficient conversion because, in high index contrast platforms, the longitudinal components can be almost as large as their transverse counterparts [18]. Importantly, longitudinal components have a spatial distribution that is distinct from, but linked to, that of the principal transverse component [13]. In the case of phase matching to a TM_{01} mode, both terms of Eq. (7) are large because the involved spatial distributions are very similar to each other. This is made possible by the very large index contrast of the platform and highlights the strong potential of type II phase matching for SHG in III-V-on-insulator wire waveguides.

Next we aim to experimentally confirm this large theoretical conversion efficiency.

We fabricate InGaP-on-insulator waveguides through wafer bonding [19]. The starting epitaxial stack is made of a 350 µm substrate of AlGaAs, a 200 nm sacrificial layer of InGaP, another 200 nm sacrificial layer of AlGaAs, and then a 320 nm InGaP layer. A thin layer of 15 nm silicon oxide is deposited on top of the stack to improve adhesion. The stack is then bonded on an oxidized silicon wafer (3 µm SiO_2) using a BenzoCycloButene (BCB) dilution as an adhesive layer. We remove the substrate with a $HNO_3 : H_2O_2 : H_2O$ solution in a 1:4:1 proportion and pattern waveguides using electron-beam lithography. A negative resist (HSQ) is deposited prior to illumination. The waveguides are patterned using inductively coupled plasma etching. The HSQ layer is not removed after etching, resulting in a 200 nm cladding.

The width of the waveguides, characterized with scanning electron microscopy, is 850 nm. In this structure, the efficient conversion to a TM_{01} SH mode, as discussed above, is predicted to occur for a pump wavelength of 1536 nm (Fig. 2). The corresponding theoretical effective nonlinearity is $\kappa_{12} = i3200(\sqrt{\mathrm{W}} \cdot \mathrm{m})^{-1}$. We design waveguides made of three sections of different directions [Fig. 3(b)]. This is because the cleave direction of both silicon and III-V semiconductors are at 45° (i.e., along the [101] and [$\bar{1}$01] axes). The main section, located in the middle, is aligned with a crystallographic axis. It is connected, on both ends, to sections normal to cleavage planes to facilitate light injection and collection. A 5 µm wide and 200 µm long taper is used at the input to optimize the injection. The middle section is 1.4 mm long, and the total length is 4.5 mm.

The experimental setup is depicted in Fig. 3(a). We inject the light using a lensed fiber. The coupling loss is estimated at 6 dB. A polarization controller allows us to tune the input polarization state. The light is collected from the waveguide with a high NA objective (0.9). The pump and SH wavelengths are separated with a dichroic mirror and sent through a Glan–Taylor polarizer to a photodiode. To characterize the SH (pump) diffusion pattern, we image the chip from the top with a silicon (InGaAs) camera. In the first experiment, we inject 25 mW from a C-band laser and tune both the input wavelength and polarization. As predicted, the brightest pattern is found at 1536 nm when both TE_{00} and a TM_{00} pump modes are simultaneously excited. The output SH wave is predominantly vertically polarized, as

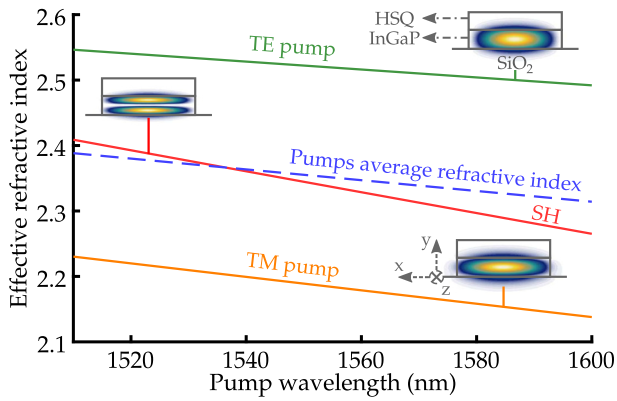

Fig. 2. Effective refractive indices of the pump and SH modes of a 850 nm wide and 320 nm high InGaP-on-insulator wire waveguide with a 200 nm cladding layer as a function of the pump wavelength. The corresponding Poynting vector distributions are also shown. The average of the indices of the two pump fundamental modes is plotted to highlight the phase matching point.

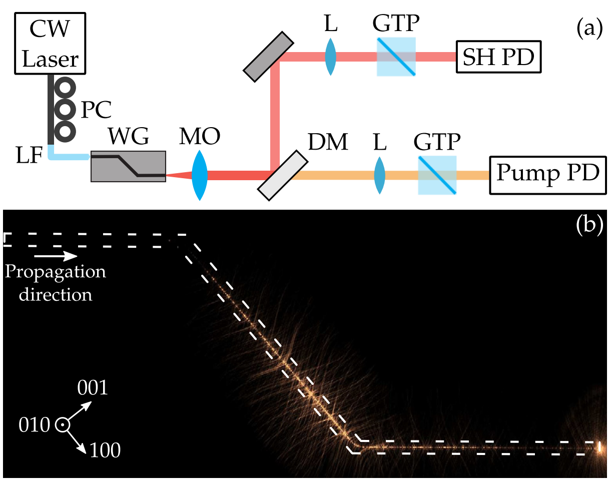

Fig. 3. (a) Experimental setup. A continuous wave (CW) laser goes through a polarization controller (PC) before being injected in the waveguide (WG) due to a lensed fiber (LF). The light is collected with a microscope objective (MO) before being split by a dichroic mirror (DM). Each wave goes through an imaging lens (L) and a Glan–Taylor polarizer (GTP). The power is finally measured by a dedicated photodiode (PD). (b) Top view of the waveguide as captured with a silicon camera.

expected. The corresponding SH diffusion pattern is shown in Fig. 3(b). We see that the SH appears at the beginning of the middle section, the one aligned with a crystallographic axis. The SH intensity increases until the second bend, after which it decays, as expected from the lack of nonlinear coupling in waveguides rotated at 45° from a crystallographic axis. To extract the experimental effective nonlinearity (κ_{exp}), we estimate the loss at each wavelength by fitting diffusion patterns. For the pump modes, we perform an experiment at low power, and for the SH TM_{01} mode, we use the last section of the waveguide where no SH conversion occurs. We find 1.2 dB/mm for the pump modes and 6.4 dB/mm at the SH, corresponding to $L_{\mathrm{eff}} = 700$ µm. An injected input power of 25 mW corresponds to 3.8 mW at the beginning of the 0° section. Because it is difficult to experimentally evaluate the outcoupling loss for the SH mode, we

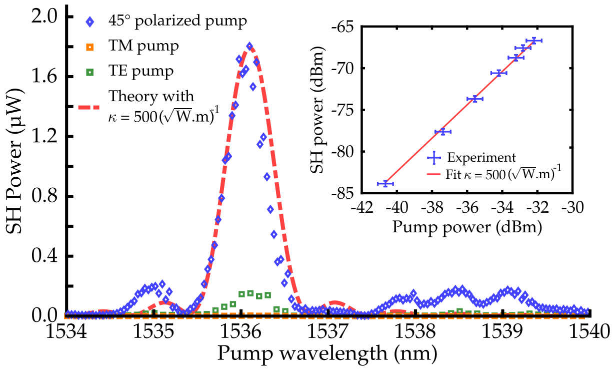

Fig. 4. Experimental SH power as a function of the pump wavelength for a purely TE pump (green squares), a purely TM pump (orange squares), and a hybrid pump (blue diamonds). The red dashed line corresponds to the theoretical output SH power. The inset shows the measured (blue crosses) and fit (red line) of the SH power as a function of the input power.

consider that we collect all the output power and hence give a lower bound of the experimental effective nonlinearity. We first extract κ_{exp} from the output SH power at the phase matching wavelength and next characterize the spectral transmittance of the process.

The maximum output SH power (at $\lambda_p = 1536$ nm) as a function of the input power is shown in the inset of Fig. 4. It is fitted with the theoretical function $P_{\mathrm{sh}} = |\kappa_{\mathrm{exp}} P_0 L_{\mathrm{eff}}|^2$ that allows us to extract the conversion efficiency value. We find $|\kappa_{\mathrm{exp}}| > 500(\sqrt{\mathrm{W}} \cdot \mathrm{m})^{-1}$. The recorded output SH power as a function of input wavelength for three different input polarization states is shown in Fig. 4 and confirms that the process is more efficient when both input modes are equally excited. Also plotted is the theoretical transfer function Eq. (4) computed for $|\kappa_{\mathrm{exp}}| = 500(\sqrt{\mathrm{W}} \cdot \mathrm{m})^{-1}$. The agreement between the theoretical spectral acceptance and our experimental results is excellent.

The maximum conversion efficiency, defined as $|\kappa_{\mathrm{exp}}|^2$, is equal to $2500\%/(\mathrm{W} \cdot \mathrm{cm}^2)$, which corresponds to 12%/W in our waveguide. It is similar to recently reported values in lithium niobate [$2600\%/(\mathrm{W} \cdot \mathrm{cm}^2)$] [20], but it is an order of magnitude lower than the record $47,000\%/(\mathrm{W} \cdot \mathrm{cm}^2)$ efficiency recently obtained in GaAs nanowaveguides [5]. Yet, the theoretical limit in our case, corresponding to $|\kappa_{12}|^2$, is $102,400\%/(\mathrm{W} \cdot \mathrm{cm}^2)$. It highlights the strong potential of type II SHG for future integrated frequency converters. InGaP wire waveguides with much lower propagation loss should hence permit converting as little as 1 μm into 1 nW of SH power in a 1 cm long waveguide. Encouragingly, several demonstrations of low loss III-V semiconductor waveguides have been recently reported [21,22].

In conclusion, we demonstrated efficient type II SHG in InGaP nanowires. We performed a full-vectorial theoretical analysis and showed that the most efficient conversion occurs in waveguides aligned with a crystallographic axis. In that configuration, the nonlinear coupling is enabled by longitudinal field components of both a pump mode and the SH mode. We confirmed our prediction experimentally by demonstrating very efficient conversion in an 850 nm wide, 320 nm thick wire waveguide. As predicted, the conversion is maximized when the two fundamental modes at the pump wavelength are equally excited, and the conversion occurs in a waveguide aligned with a main crystallographic axis. These results demonstrate the potential of type II phase matching to maximize the conversion in III-V semiconductor nanowaveguides, which we expect to play a role in future quantum circuits [23] and frequency comb stabilization devices [24,25].

Funding. European Research Council (726420, 757800, 759483); Fonds De La Recherche Scientifique - FNRS (PDR.T.0.185.18).

Disclosures. The authors declare no conflicts of interest.

REFERENCES

1. P. A. Franken, A. E. Hill, C. W. Peters, and G. Weinreich, Phys. Rev. Lett. **7**, 118 (1961).
2. K. Schneider, P. Welter, Y. Baumgartner, H. Hahn, L. Czornomaz, and P. Seidler, J. Lightwave Technol. **36**, 2994 (2018).
3. J. S. Levy, M. A. Foster, A. L. Gaeta, and M. Lipson, Opt. Express **19**, 11415 (2011).
4. A. D. Logan, M. Gould, E. R. Schmidgall, K. Hestroffer, Z. Lin, W. Jin, A. Majumdar, F. Hatami, A. W. Rodriguez, and K.-M. C. Fu, Opt. Express **26**, 33687 (2018).
5. E. J. Stanton, J. Chiles, N. Nader, G. Moody, N. Volet, L. Chang, J. E. Bowers, S. Woo Nam, and R. P. Mirin, Opt. Express **28**, 9521 (2020).
6. N. Singh, M. Raval, A. Ruocco, and M. R. Watts, Light Sci. Appl. **9**, 17 (2020).
7. M. Bartnick, M. Santandrea, J. P. Hoepker, F. Thiele, R. Ricken, V. Quiring, C. Eigner, H. Herrmann, C. Silberhorn, and T. J. Bartley, "Cryogenic second harmonic generation in periodically-poled lithium niobate waveguides," arXiv:2005.07500 (2020).
8. R. Luo, Y. He, H. Liang, M. Li, and Q. Lin, Laser Photon. Rev. **13**, 1800288 (2019).
9. E. Nitiss, T. Liu, D. Grassani, M. Pfeiffer, T. J. Kippenberg, and C.-S. Brès, ACS Photon. **7**, 147 (2020).
10. D. Duchesne, K. A. Rutkowska, M. Volatier, F. Légaré, S. Delprat, M. Chaker, D. Modotto, A. Locatelli, C. De Angelis, M. Sorel, D. N. Christodoulides, G. Salamo, R. Arès, V. Aimez, and R. Morandotti, Opt. Express **19**, 12408 (2011).
11. N. Poulvellarie, U. Dave, K. Alexander, C. Ciret, M. Billet, C. Mas Arabi, F. Raineri, S. Combrié, A. De Rossi, G. Roelkens, S.-P. Gorza, B. Kuyken, and F. Leo, Phys. Rev. A **102**, 023521 (2020).
12. C. Ciret, K. Alexander, N. Poulvellarie, M. Billet, C. Mas Arabi, B. Kuyken, S.-P. Gorza, and F. Leo, Opt. Express **28**, 31584 (2020).
13. A. W. Snyder and J. Love, *Optical Waveguide Theory* (Chapman and Hall, 1983).
14. S. Afshar and T. M. Monro, Opt. Express **17**, 2298 (2009).
15. L. Alloatti, D. Korn, C. Weimann, C. Koos, W. Freude, and J. Leuthold, Opt. Express **20**, 20506 (2012).
16. M. Kolesik and J. V. Moloney, Phys. Rev. E **70**, 036604 (2004).
17. Y. Ueno, V. Ricci, and G. I. Stegeman, J. Opt. Soc. Am. B **14**, 1428 (1997).
18. J. B. Driscoll, X. Liu, S. Yasseri, I. Hsieh, J. I. Dadap, and R. M. Osgood, Opt. Express **17**, 2797 (2009).
19. U. D. Dave, B. Kuyken, F. Leo, S.-P. Gorza, S. Combrie, A. De Rossi, F. Raineri, and G. Roelkens, Opt. Express **23**, 4650 (2015).
20. C. Wang, C. Langrock, A. Marandi, M. Jankowski, M. Zhang, B. Desiatov, M. M. Fejer, and M. Lončar, Optica **5**, 1438 (2018).
21. L. Ottaviano, M. Pu, E. Semenova, and K. Yvind, Opt. Lett. **41**, 3996 (2016).
22. L. Chang, W. Xie, H. Shu, Q.-F. Yang, B. Shen, A. Boes, J. D. Peters, W. Jin, C. Xiang, S. Liu, G. Moille, S.-P. Yu, X. Wang, K. Srinivasan, S. B. Papp, K. Vahala, and J. E. Bowers, Nat. Commun. **11**, 1331 (2020).
23. S. Zaske, A. Lenhard, C. A. Keßler, J. Kettler, C. Hepp, C. Arend, R. Albrecht, W.-M. Schulz, M. Jetter, P. Michler, and C. Becher, Phys. Rev. Lett. **109**, 147404 (2012).
24. S. A. Diddams, D. J. Jones, J. Ye, S. T. Cundiff, J. L. Hall, J. K. Ranka, R. S. Windeler, R. Holzwarth, T. Udem, and T. W. Hänsch, Phys. Rev. Lett. **84**, 5102 (2000).
25. Y. Okawachi, M. Yu, B. Desiatov, B. Y. Kim, T. Hansson, M. Lončar, and A. L. Gaeta, Optica **7**, 702 (2020).